Journal Pre-proof

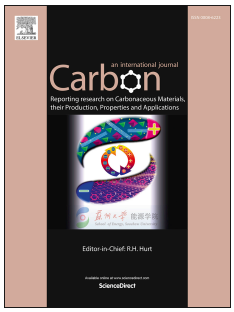

Joule-heat derived amorphous/graphitic polymer nanotubes with enhanced electromagnetic wave absorption and high thermal conductivity

Yan Cao, Xinfei Zeng, Jingtao Su, Wentao Yu, Haichen Zhang, Safaa N. Abdou, Mohamed M. Ibrahim, Ahmed M. Fallatah, Jing Zhang, Nurgul Amangeldi, Hassan Algadi, Yerezhepova Ainur, Zhexenbek Toktarbay, Jintao Huang, Yonggang Min, Zhanhu Guo

PII: S0008-6223(25)00443-9

DOI: https://doi.org/10.1016/j.carbon.2025.120427

Reference: CARBON 120427

To appear in: *Carbon*

Received Date: 10 March 2025

Revised Date: 8 May 2025

Accepted Date: 13 May 2025

Please cite this article as: Y. Cao, X. Zeng, J. Su, W. Yu, H. Zhang, S.N. Abdou, M.M. Ibrahim, A.M. Fallatah, J. Zhang, N. Amangeldi, H. Algadi, Y. Ainur, Z. Toktarbay, J. Huang, Y. Min, Z. Guo, Joule-heat derived amorphous/graphitic polymer nanotubes with enhanced electromagnetic wave absorption and high thermal conductivity, *Carbon*, https://doi.org/10.1016/j.carbon.2025.120427.

Graphical Abstract

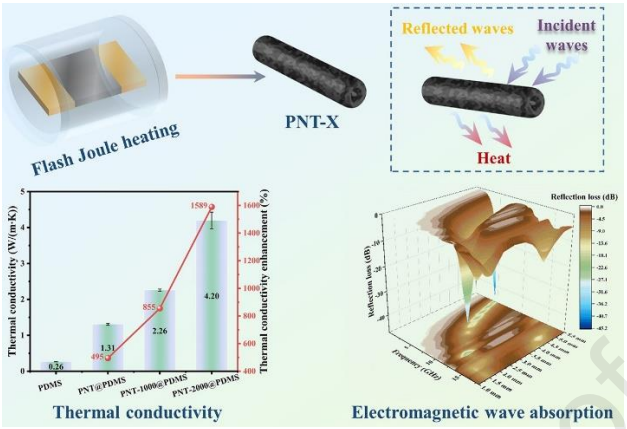

Joule-heat derived amorphous/graphitic polymer nanotubes with enhanced electromagnetic wave absorption and high thermal conductivity

Yan Cao[a], Xinfei Zeng[a], Jingtao Su[a], Wentao Yu[a], Haichen Zhang[d], Safaa N. Abdou[b], Mohamed M. Ibrahim[c], Ahmed M. Fallatah[c], Jing Zhang[e,j], Nurgul Amangeldi[f], Hassan Algadi[i], Yerezhepova Ainur[g], Zhexenbek Toktarbay[h], Jintao Huang[a*], Yonggang Min[a*], Zhanhu Guo[e*]

[a] Department of Polymeric Materials and Engineering, School of Materials and Energy, Guangdong University of Technology, Guangzhou 510006, China.

[b] Department of Chemistry, Khurmah University College, Taif University, Taif, Saudi Arabia.

[c] Department of Chemistry, College of Science, Taif University, P.O. Box 11099, Taif, 21944, Saudi Arabia

[d] School of Materials Science and Hydrogen Energy, Foshan University, Foshan 528000, China.

[e] Department of Mechanical and Construction Engineering, Faculty of Engineering and Environment, Northumbria University, Newcastle Upon Tyne NE1 8ST, UK

[f] Department of Pre-University Training, Faculty of Pre-University Education, Al-Farabi Kazakh National University, Al-Farabi Av. 71, Almaty 700420, Kazakhstan.

[g] Department of Chemistry, Faculty of Natural Science, Kazakh National Woman's Teacher Training University, Aitekebi Street 99, Almaty 700420, Kazakhstan.

[h] Department of Chemistry, Faculty of Natural Sciences and Geography, Abai Kazakh National Pedagogical University, 13 Dostyk Ave., Almaty 050010, Kazakhstan

i Department of Electrical Engineering, Faculty of Engineering, Najran University, Najran, 11001, Saudi Arabia

[j] *College of Chemical Engineering and Technology, Taiyuan University of Science and Technology, Taiyuan, 030024, China*

* Corresponding author: jintao.huang@gdut.edu.cn (J. Huang), ygmin@gdut.edu.cn (Y. Min), zhanhu.guo@northumbria.ac.uk (Z. Guo).

Abstract

The rapid advancement of artificial intelligence demands multifunctional materials integrating electromagnetic wave absorption (EWA) and thermal management capabilities for next-generation electronics. Herein, a facile and scalable Joule-heating carbonization strategy is proposed to regulate the amorphous-to-graphitic phase ratio in polymer nanotubes, achieving a precise modulation of EWA performance. The nitrogen species transformation during carbonization induced enhanced polarization relaxation, defect generation, and dipole polarization, synergistically facilitating charge transfer. Polypyrrole-based polymer nanotubes treated at 1000 ^{o}C (PNT-1000) exhibited a maximum effective absorption bandwidth of 3.46 GHz and a minimum reflection loss of −45.1 dB. Moreover, PNT-1000@polydimethylsiloxane (PDMS) demonstrated a thermal conductivity of 2.26 W/(mK), while PNT-2000@PDMS achieved a significantly higher thermal conductivity of 4.20 W/(mK). This work systematically elucidated the interaction between amorphous and graphitic phases in controlling both EWA and thermal conductivity, which is helpful for applying carbon-based materials in these advanced fields.

Keywords: Joule-heat-driven, amorphous, graphitized, nanotubes, electromagnetic wave absorbers.

1. Introduction

The rapid advancement of artificial intelligence (AI) technologies has led to a proliferation of AI-enabled products and services [1, 2], while simultaneously drives the development of high-performance electronic devices [3-6]. Meanwhile, electromagnetic wave (EMW) has demonstrated a broad scope of applications [7-10] and energy usage [11, 12]. However, this development has introduced serious issues of EMW radiation pollution and misfunction/dysfunction induced by the thermal effects in electronic devices [13, 14]. These issues not only pose a threat to production safety but also endanger human health [15, 16]. While EMW absorbers effectively dissipate incident radiation that converts them into thermal energy, this will accelerate heat accumulation in devices [17, 18]. Therefore, it is extremely urgent to develop materials with a synergistic effect of microwave absorption and thermal management.

To overcome these challenges, a variety of materials with electromagnetic wave absorption (EWA) properties have been developed [19-21]. Among these, carbon materials and magnetic materials have garnered significant attention [22-24]. Carbon materials, in particular, are considered indispensable due to their low mass density, high mechanical strength, and minimal environmental impact [25, 26]. These materials exhibit diverse nanostructural configurations, including hollow carbon nanospheres [27], carbon nanotubes (CNT) [28-30], graphene [31-33], and porous carbon [34, 35]. Ge et al. [36] proposed to prepare a flexible film composed of 0.2 vol% single-walled carbon nanotubes (SWCNT), 70 vol% polyethylene glycol (PEG) and polydimethylsiloxane (PDMS). This film achieved a microwave attenuation of −20 dB and a

thermal conductivity of 0.524 W/(m·K). In this, the SWCNT was immobilized in the PDMS to form a good thermal conductivity path. Lin et al. [37] developed a heterogeneous structure containing cobalt (Co)@carbon nanotubes (CNT)/boron nitride flakes (BNFs). This structure demonstrated exceptional EWA, with a minimal reflection loss (RL) of −46.6 dB and an extensive effective absorption bandwidth (EAB) spanning 5.92 GHz. Additionally, when the composite was blended with PDMS at a 30 wt% filler ratio, the resulting material exhibited a thermal conductivity of 0.72 W/(m·K). The CNTs, which were grown directly on the BNF surfaces, established interconnected thermal conduction pathways through direct contact with the BNFs. These interactions facilitated the formation of localized thermal networks and bridging configurations, thereby enhancing continuous heat transfer across the composite [38]. Dai et al. [39] demonstrated that the heat treatment temperature has a significant effect on the performance of carbon fibers, and optimal EWA performance (−44.44 dB) was achieved at 850 ºC by introducing boundary-type graphite defects to enhance the interfacial polarization loss, conductive loss and eddy current loss. Similarly, Xu et al. [40] exhibited that Zn, N doping in carbon materials leads to electron cloud distortion and defect generation, which improves the interfacial polarization and achieves an EAB of 5.89 GHz at a thickness of 2 mm. Although achievements have been made in the EWA performance of various carbon-based materials, there is an overall lack of systematic research on the absorption mechanisms of carbon materials prepared at different temperatures. Moreover, the existing thermal conductivity may not meet the requirements of high-demand scenarios. This may limit the further optimization of their performance and the expansion of their applications.

Conventional carbonization and graphitization treatment methods often encounter challenges like long production cycles and high costs. Thus, there is an urgent need to develop a rapid and efficient heat treatment technique, especially in the fields of EWA and thermal regulation. Recently, microwave heating [41-43] and Joule heat-driven [44, 45] carbon thermal shock methods, which are capable of instantly elevating the surface temperature of carbon materials to approximately 3000 K, have emerged as promising approaches. While microwave heating relies on dielectric polarization effects to generate internal heat through molecular friction with an energy efficiency of 60 ~ 70% [46]. However, Joule heating utilizes electrical resistance to convert electrical energy directly into thermal energy (energy conversion efficiency >95%) [47] and achieves precise control through adjustable current parameters to achieve targeted phase transitions [48]. This creates essential conditions for the investigation of amorphous and graphitized materials.

In this work, we proposed a straightforward carbonization strategy to regulate the proportion of amorphous and graphitized components in polypyrrole-based polymer nanotubes (PNT). By applying rapid Joule heating to raise the processing temperature, we observed that the amorphous-to-graphite ratio decreased gradually. This transition was accompanied by increased conductivity loss and polarization loss, ultimately optimizing the overall EWA performance. Among them, PNT-1000 exhibited excellent EWA performance. It achieved 90% absorption performance within the frequency range of 2 − 18 GHz with varying thicknesses. Moreover, due to the enlarged grain size, when PNT-2000 was blended with PDMS, it presented a thermal conductivity as high as 4.20

W/(m·K), which is 1589% that of pure PDMS. The roles of amorphous and graphitized polymer nanotubes in coordinating EWA performance and thermal management clarify, making it possible for carbon materials to be more widely applied in addressing EWA radiation pollution and thermal effects.

2. Experimental

PNT was synthesized via a template method [49]. First, methyl orange powder was dissolved. Then, $FeCl_3$ was added, followed by the introduction of pyrrole (Py) in an ice-water bath. This process led to the formation of a black precipitate, which was subsequently washed and dried to obtain PNT. By employing Flash Joule Heating, PNT was thermally shocked at different target temperatures (700 ~ 2800 ºC) in argon (Fig. 1 (a) and Fig. S1). PNT-X@PDMS composites were prepared by mixing 10 wt% PNT-X with PDMS. The mixture was cast into a thin film and thermally cured to obtain the final composite material. More experimental details are provided in the Supporting Information section.

3. Results and discussion

3.1. Morphological evolution from PNT to PNT-X

The morphologies of PNT and PNT-X (X = 700 ~ 2800 ºC) were studied by SEM. Fig. 1 (b) shows that PNTs are tubular structures with a diameter of about 300 nm. In addition to morphology, the elemental distribution in PNT was also investigated. Fig. S2 clearly shows the distributions of major elements C (46.7 wt.%), N (17.8 wt.%) and O (33.4 wt.%) in PNT. Fig. 1 (c ~ j) shows the morphology of PNT-X at thermal shock temperatures from 700 ºC to 2800 ºC. Obviously, as the

thermal shock temperature increases, the morphology gradually changes. The diameter ranges from 180 ~ 310 nm, and the length is several microns (Fig. S3). Up to 2400 ºC, the hollow tubular structure is retained, but at 2600 ºC, cracks begin to appear in the tubes. At 2800 ºC, the tubular structure is evidently destroyed and transforms into a sheet-like structure. Thus, the gradual morphological transition of PNT-X from a hollow tubular to a lamellar structure with increasing thermal shock temperature suggests a gradual reorganization of amorphous carbon into graphitic carbon. This will be further confirmed by X-ray diffractometer (XRD) and Raman in the subsequent sections.

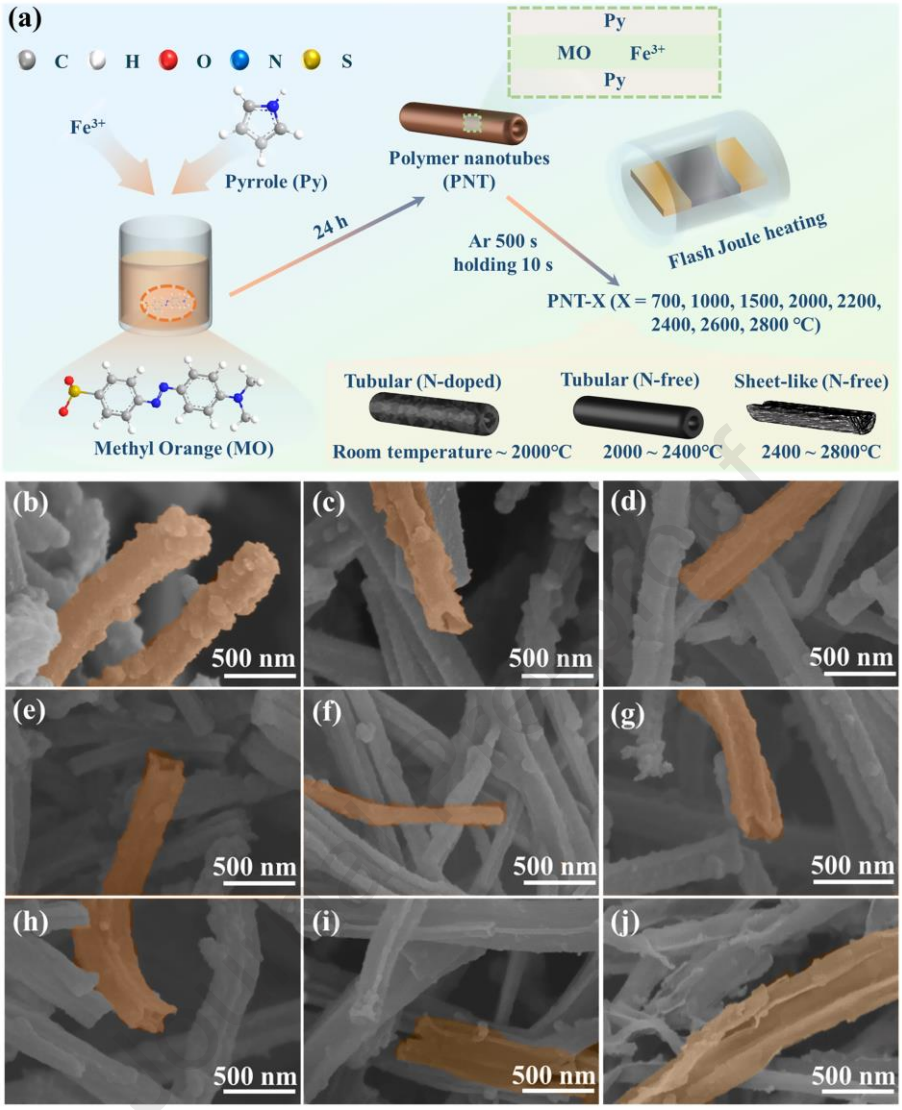

Fig. 1. (a) Schematic diagram of the preparation of PNT-X. SEM image of (b) PNT, (c) PNT-700, (d) PNT-1000, (e) PNT-1500, (f) PNT-2000, (g) PNT-2200, (h) PNT-2400, (i) PNT-2600, and (j) PNT-2800.

3.2. Characterization and analysis of PNT and PNT-X

As illustrated in Fig. S4, the Fourier transform infrared spectra of PNT exhibit characteristic absorption bands. The peaks at 1550 and 1462 cm^{-1} correspond to the stretching vibrations of C−C and C=N bonds within the pyrrole ring [50]. Additionally, the spectral features at 1310 and 1040 cm^{-1} likely arise from in-plane C−H vibrational modes, while the absorption band at 1180 cm^{-1}

can be assigned to C−N bond stretching vibrations [51]. To investigate chemical states and crystal structural evolution, XRD and Raman analyses were performed on all samples. As shown in Fig. 2 (a), PNT has a broad peak scattering, which indicates that it is a highly amorphous structure, corresponding to the characteristic peak of PPy [52]. In the temperature range of 700 ~ 1000 °C, the diffraction peaks narrow. Nevertheless, the crystallinity remains low, with a large proportion of amorphous carbon present. In the temperature range from 1500 °C to 2800 °C, PNT-X show a gradually sharp peak in the range of 25.68° ~ 26.36°, which is the carbon (002) peak [53], indicating a high degree of crystallinity. Besides the strong (002) peak, the samples at 2400 °C, 2600 °C, and 2800 °C also exhibit small peaks at 2 θ = 42.50° and 53.58°, which may be ascribed to the diffraction peaks of the (101) and (004) graphite planes, respectively [54]. As the heat treatment temperature increases, the graphite crystallite diameters of PNT-X along the a-axis (L_a, 27.47 nm) and the c-axis (L_c, 13.29 nm) increase, which confirms that the graphitization rate of PNT-X becomes higher (Fig. 2 (b)). Interestingly, as the graphitization rate of PNT-X increases, starting from PNT-2200, the interlayer distance (d_{002}) decreases from 0.35 nm to 0.34 nm. Table 1 lists the XRD-related parameters. The crystallization parameters can be calculated using the Bragg equation [55]. The structure parameters of graphite-like microcrystals (G) can be derived from the Mering-Maire formula [56, 57], and the crystallite size L_a and L_c, can be determined by the following equations [58, 59]:

$$\lambda = 2d_{002} \sin\theta \quad (1)$$

$$G = \frac{0.3440 - d_{002}}{0.3440 - 0.3354} \times 100\% \quad (2)$$

$$L_{\mathrm{a}} = \frac{1.84\,\lambda}{\beta \cos\theta} \quad (3)$$

$$L_{\mathrm{c}} = \frac{0.89\,\lambda}{\beta \cos\theta} \quad (4)$$

where λ represents the wavelength of incident X-rays, θ denotes the Bragg angle corresponding to diffraction, β corresponds to the full width at half maximum (FWHM), and d_{002} is the interplanar spacing of the (002) plane.

The graphite-like microcrystals (G) of PNT-2400, PNT-2600 and PNT-2800 is 36.2%, 59.9% and 68.7%, respectively. The results show that PNT-X with a thermal shock temperature of 2400 °C and above does have a high degree of graphitization. However, SEM images show that the tubular morphology of PNT-2600 and PNT-2800 has been destroyed. Consequently, subsequent tests on these two samples were not conducted.

Table 1.

The related parameters of XRD results.

Samples	2θ (°)	β	d_{002} (nm)	L_{a} (nm)	L_{c} (nm)	G (%)
PNT-700	25.26	0.161	0.35	1.80	0.87	-
PNT-1000	25.52	0.121	0.35	2.40	1.16	-
PNT-1500	25.68	0.083	0.35	3.50	1.69	-
PNT-2000	25.82	0.044	0.35	6.53	3.16	-
PNT-2200	25.88	0.042	0.34	6.89	3.33	-

PNT-2400	26.14	0.026	0.34	10.98	5.31	36.2
PNT-2600	26.30	0.012	0.34	24.03	11.62	59.9
PNT-2800	26.36	0.010	0.34	27.47	13.29	68.7

Further, the degree of graphitization of PNT-X was determined by Raman spectroscopy. The Raman spectra in Fig. 2 (c) reveal characteristics of PNT, with prominent peaks at 1367 and 1580 cm^{-1} corresponding to C−C and C=C stretching vibrations in the polymer backbone [60]. PNT-X at 700 ~ 2400 ºC shows obvious peaks at 1350 and 1580 cm^{-1}. These features evolve into the disorder-induced D band and graphitic G band, respectively [61]. The D band originates from structural defects, while the G band represents sp^2-hybridized carbon domains [62]. As the temperature rises, the intensity of the G peak increases, indicating an increasing degree of graphitization of the sample. The graphitization degree was assessed using the intensity ratio (I_D/I_G), as presented in Fig. 2 (d). The I_D/I_G values decrease from 1.52 (PNT-700) to 0.39 (PNT-2400), demonstrating an improved structural ordering at higher carbonization temperatures. This correlation between I_D/I_G ratio and treatment temperature confirms the thermally driven graphitization process, which aligns well with the structural evolution observed in XRD patterns.

The formation process of PNT-X was investigated by thermogravimetric analysis (TGA). Fig. 2(e) shows that all samples exhibited a slight mass reduction at 100 ºC, attributable to the desorption of physically adsorbed water molecules from the samples. In the temperature range of 300 to 400 ºC, the rapid weight loss of PNT indicates the onset of its initial carbonization stage. As the temperature increases to 700 ºC, the further decomposition of PNT leads to a decrease in

the final carbon content to 53.3%. Notably, as the carbonization temperature continues to increase, the residual carbon content of PNT-X rises significantly. The residual carbon content of PNT-700 at 800 ºC is 86.3%, while the carbon contents of PNT-1500 and PNT-2000 reach 92.6% and 95.5%, respectively. This trend correlates with progressive graphitization, as evidenced by PNT-2400 showing no further mass loss. Consequently, the observed mass reduction occurring between 300 and 800 ºC corresponds principally to PPy thermal degradation, which produces multiple nitrogenous compounds including HCN, NH_3, and N_2 gaseous species. This decomposition process leads to a progressive reduction in the N/C atomic ratio within the carbonized tubular structures [63]. These findings demonstrate that elevated carbonization temperatures promote more complete carbonization of the material, ultimately driving the structural evolution toward graphitic ordering.

In addition, the electrical conductivity of PNT and PNT-X were measured using the four-probe method, and the results are presented in Fig. 2 (f). Below 1000 ºC, PNT, PNT-700, and PNT-1000 exhibit a linear conductivity increasing from 18.56 to 32.92 S/m with rising treatment temperature. When the heat treatment temperature ranges from 1000 ºC to 2000 ºC, the electrical conductivity of PNT-X shows a steeper increasing trend. Specifically, the electrical conductivity of PNT-2000, PNT-2200 and PNT-2400 are 1114, 1224 and 1416 S/m, respectively. This phenomenon can be attributed to the fact that, as shown in the data of Fig. 2 (b), the L_a of the PNT-X material exhibits a gradient increase with increasing heat treatment temperature: from 2.4 nm at 1000 ºC to 10.98 nm at 2400 ºC. It is noteworthy that the increase in L_a reaches a factor of

2.7 in the interval of 1000 − 2000 ºC, whereas the increase slows down to a factor of 1.7 in the interval of 2000 − 2400 ºC. This pre-fast growth characteristic is directly related to the steep trend of conductivity increase. The expansion of grain size promotes electron transport along the graphene planes [64], thus contributing to the increase in electrical conductivity.

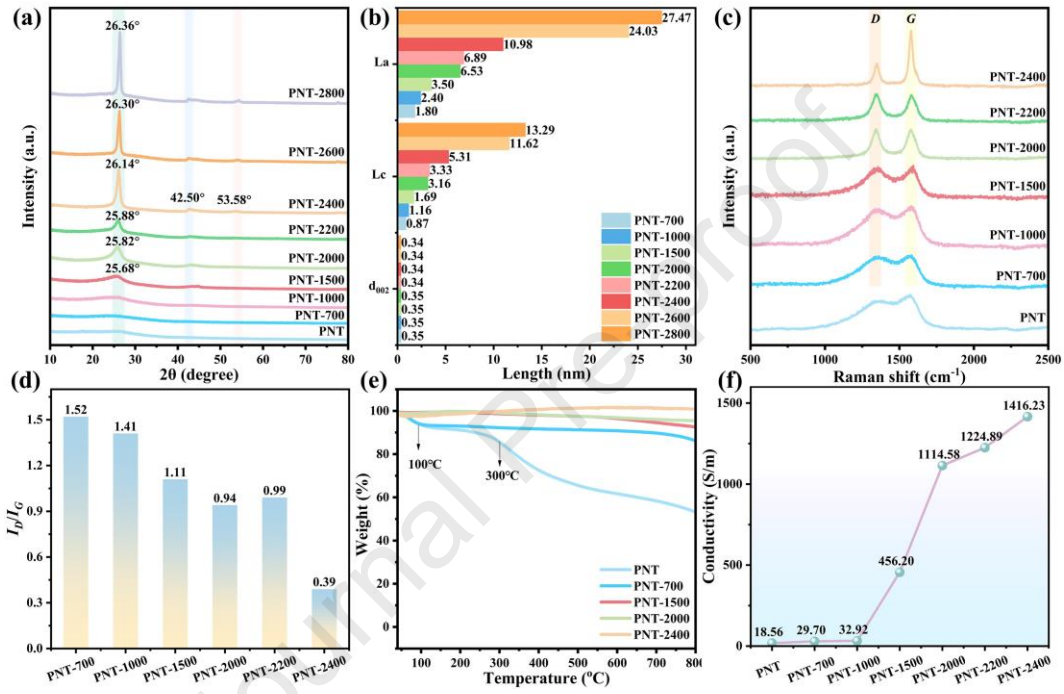

Fig. 2. (a) XRD patterns, (b) L_a, L_c, and d_{002} of PNT-X, (c) Raman spectra, (d) I_D/I_G, (e) TGA, and (f) electrical conductivity of samples.

According to Fig. S5, C 1s X-ray photoelectron spectroscopy (XPS) spectra are divided into four peaks. The peaks at 284.0 and 284.9 eV both correspond to C=C configurations, while the higher binding energy components at 285.7 and 287.1 eV are characteristic of C−N and C−O bonds, respectively [65]. These are the characteristic peak of PNT. In addition, XPS analysis shows that PNT-700 (Fig. 3 (a_1)) and PNT-1500 (Fig. 3 (b_1)) are mainly composed of C, N and O. Their binding energies are concentrated at 285.0, 400.0 and 531.0 eV, corresponding to C 1s, N 1s and

O 1s respectively. PNT-2000 (Fig. 3 (c_1)) and PNT-2400 (Fig. 3 (d_1)) mainly consist of C and O. Notably, as the processing temperature rises, the intensity of N 1s gradually declines, suggesting the removal of heteroatoms and the formation of graphite. Specifically, the C 1s spectrum of PNT-700 reveals the dominant peak at 284.7 eV represents graphitic C=C bonds, while the subsequent peaks correspond to C−C (285.7 eV), C−N (287.1 eV), and O−C=O (288.8 eV) groups (Fig. 3 (a_2)). From PNT-700 to PNT-2400 (Fig. 3 (a_2 ~ d_2), the increase in the strength of the C=C bond indicates a rise in the content of graphitic carbon within the tubular structure of PNT–X, signifying a transformation from amorphous carbon to a graphitic structure. As shown in Fig. 3 (a_3, b_3), the N 1s spectra of PNT-700 and PNT-1500 are divided into three bands at 398.2, 400.6, and 403.6 eV, which are attributed to pyrrolic N, graphitic N, and nitrogen–oxygen bonds, respectively [66]. Graphitic N, located in the graphite plane, has greatly enhanced stability. In contrast, pyrrolic N, situated in the edge region, has defects, high reactivity, but low stability at high temperatures. The decrease in the intensity of pyrrolic N and the increase in that of graphitic N imply the transition from amorphous carbon to graphitic carbon. As shown in Fig. 3 (c_3, d_3), the disappearance of the N content in PNT-2000 and PNT-2400 indicates that the amorphous carbon in the samples has been completely converted into graphitic carbon, which is consistent with the above-mentioned characterization results. The increase of graphitic carbon promotes charge transport.

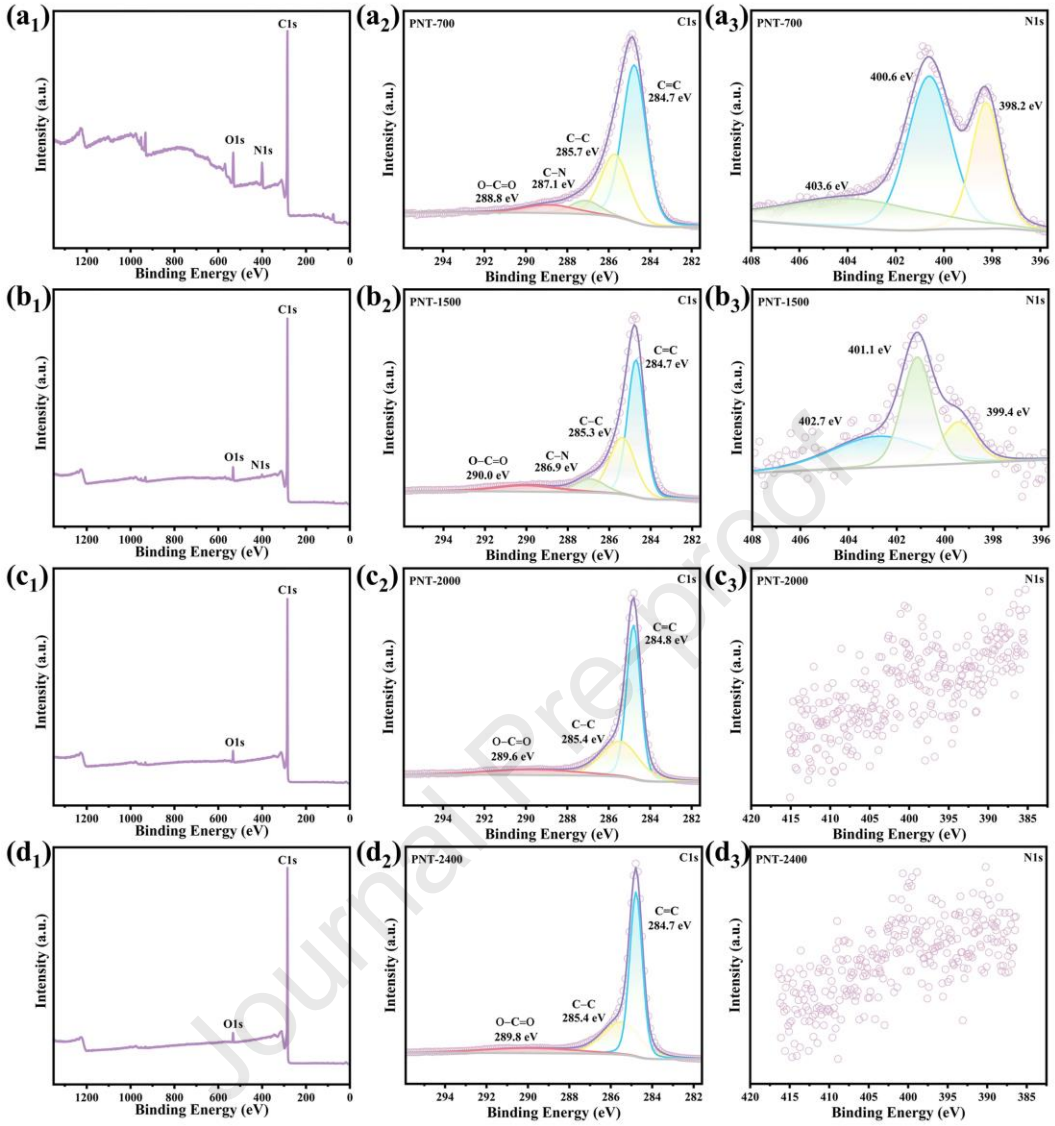

Fig. 3. XPS spectra of (a_1) PNT-700, (b_1) PNT-1500, (c_1) PNT-2000 and (d_1) PNT-2400; detailed C 1s spectra of (a_2) PNT-700, (b_2) PNT-1500, (c_2) PNT-2000 and (d_2) PNT-2400; detailed N 1s spectra of (a_3) PNT-700, (b_3) PNT-1500, (c_3) PNT-2000 and (d_3) PNT-2400.

3.3. Microwave absorption performance of PNT-X

To evaluate the EWA properties of PNT-X, we calculated the RL value. Fig. S6 (a) shows that pure paraffin wax (PW) has poor EWA performance and can be used as a benchmark for

comparison. As evidenced in Fig. S6 (b ~ d), PNT-1500, PNT-2000, and PNT-2400 exhibit RL values above −10 dB, indicating inadequate absorption performance. This means that higher carbonization temperatures lead to progressively diminished absorption capabilities across the 2−18 GHz. In contrast, as shown in Fig. 4 (a_1 ~ a_3), the PNT absorber without heat treatment exhibits relatively weak EWA performance, and its reflection loss value is approximately −18.8 dB. Subsequently, as shown in Fig. 4 (b_1 ~ b_3), it is obvious that the EWA performance of PNT-1000 has been significantly improved. Its reflection loss value has dropped to −45.1 dB, which is a significant improvement compared to the aforementioned PNT absorbers. It is worth noting that when the thickness of the PNT-1000 absorber is 1.5 mm, its optimal EAB value reaches 3.46 GHz (ranging from 14.54 to 18.00 GHz). Moreover, it should be emphasized that as the thickness of the PNT-1000 absorber changes, its reflection loss values always remain below −10 dB. This means that it can achieve 90% absorption performance in the C to Ku bandwidth [67]. In addition, the properties of pure PNT-1000 prepared by heat treatment are compared with various composites used for EWA in the literature in Table S1. The results show that PNT-1000 has superior reflection loss characteristics compared to other composites. Overall, these results strongly suggest that the prepared PNT-X, especially the outstanding PNT-1000 variant, has a strong EWA performance and a wide EAB, making it a promising material for EWA applications.

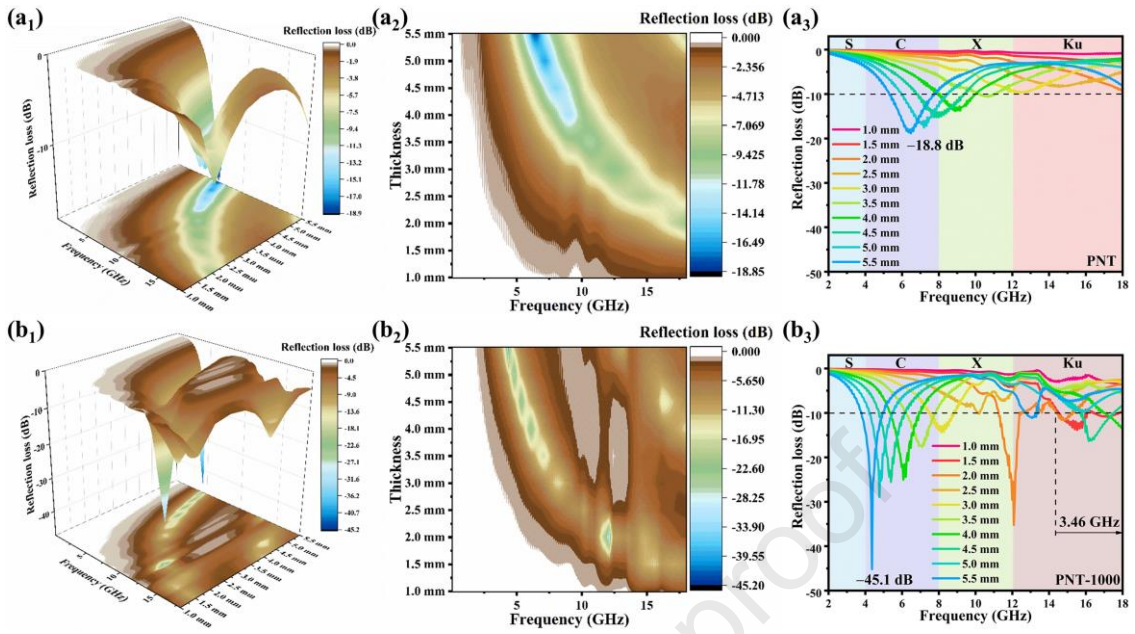

Fig. 4. RL values of the absorbers of (a_1~a_3) PNT, and (b_1~b_3) PNT-1000.

To investigate the EWA mechanism, we systematically examined the electromagnetic properties of PNT-X. The complex permittivity and permeability spectra were characterized across the 2−18 GHz microwave frequency range, with particular focus on their real (ε', μ') and imaginary (ε", μ") components. Fig. 5 (a, b) shows that the ε' and ε" values of the PNT-1000 absorber are generally higher than those of PNTs. And as shown in Fig. 2 (f), the conductivity of PNT-1000 (32 S/m) is higher than that of PNTs (18 S/m). This indicates that as the conductivity of PNT-X increases, the ability of electrons to migrate through the material is enhanced, so PNT-1000 has better electrical energy storage and dissipation capabilities. Meanwhile, Fig. 5 (c, d) shows that the μ' and μ" values of PNT and PNT-1000 absorbers are near 1 and 0, respectively. This is because the PNT-X absorber does not contain magnetic materials. Based on the Debye theory [68, 69], the relatively complex imaginary part of the dielectric constant (ε") comprises two distinct loss

mechanisms: conduction-induced losses (ε_c") and polarization-related losses (ε_p") [70, 71]. The ε_c" demonstrates a linear dependence on the absorber' electrical conductivity [72]. As the heat treatment temperature changes, the ε_c" value of the PNT-X absorber increases, indicating that the contribution of conduction loss dominates [73]. At the same time, their Cole−Cole curves all show several semicircles and irregular curves (Fig. 5 e_1~e_2), which means that when exposed to an alternating electromagnetic field, these absorbers will undergo a polarization relaxation process. Moreover, the Cole-Cole curves of PNT-1000 show more semicircles than those of PNT, implying an abundance of polarization centers. This is attributed to defects such as C-N bonds and nitrogen vacancies [74, 75]. These defects produce dipoles that align with the alternating magnetic field and dissipate energy through relaxation. The higher the concentration of defects, the stronger this process becomes, as evidenced by the complexity of the curves.

In theory, it suggests that optimal EWA materials must simultaneously satisfy excellent impedance matching characteristics and significant microwave attenuation properties [76]. From electromagnetic theory, perfect impedance matching occurs when the normalized input impedance (Z) reaches unity (Z = 1) [77]. As shown in Fig. S7 (a, b), the Z values of PNT-X absorbers at different temperatures are compared. In the low frequency range, PNT-1000 demonstrates a Z value approaching 1, significantly outperforming other samples. In contrast, the PNT exhibits consistently poor impedance matching across the entire range. This result shows that the obtained PNT-1000 has broad prospects in multi-band strong EWA applications. Based on the above results, the EWA mechanism of PNT-X is shown in Fig. 5 (f). This mechanism mainly encompasses three

aspects: multiple reflections and scattering, electron migration and transition, and dipolar polarization. When an EMW propagates in the medium and reaches the interface of PNT-1000, reflection and scattering phenomena occur. At the same time, there is an electron migration process within PNT-1000. It is worth noting that the structure of PNT-1000 is rich in dipoles. These dipoles significantly enhance the polarization relaxation phenomenon, thus enabling the material to absorb more EMW. However, as the temperature rises, the graphitization degree of PNT-X increases, and the nitrogen defects and vacancy defects decrease, which weakens the polarization relaxation and the EWA ability. From a microscopic perspective, this will reduce the number of available polarization centers. Overall, PNT-1000 shows good prospects in multi-band EWA applications.

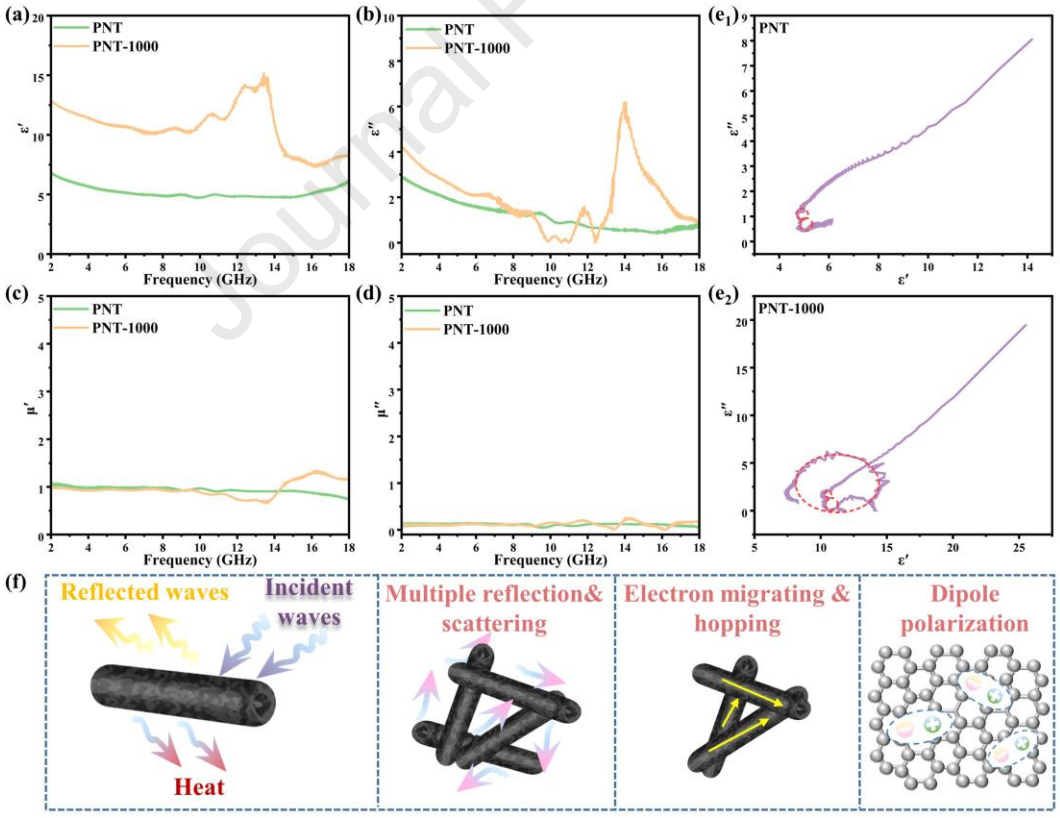

Fig. 5. (a) ε', (b) ε'', (c) μ', (d) μ''. Cole−Cole curves of (e_1) PNT and (e_2) PNT-1000. (f) EWA mechanism.

As depicted in Fig. 6 (a, b), Computer Simulation Technology (CST) was employed to conduct simulations on PW and PNT at 6.5 GHz with a thickness of 5.5 mm. The simulation results indicated that PW allowed substantial signal transmission along the Z-axis, whereas signal attenuation occurred in PNT. Fig. 6 (d, e) showed that, at a frequency of 4.3 GHz with the same thickness, the signal attenuation of PNT-1000 was more pronounced than that of PW. These results demonstrate the effective electromagnetic wave attenuation capability of PNT-X. Additionally, a detailed analysis was conducted on the angular-dependent radar cross-section (RCS) performance, as illustrated in Fig. 6 (c, f), covering incident angles from −90° to +90°. Compared with PW, the RCS values of PNT were below −10 dB m^2 throughout the entire angular range, and those of PNT-1000 were below −20 dB m^2. This simulation result was in line with the excellent EWA performance shown in Fig. 4. It further demonstrated that PNT-1000 had favorable EWA performance.

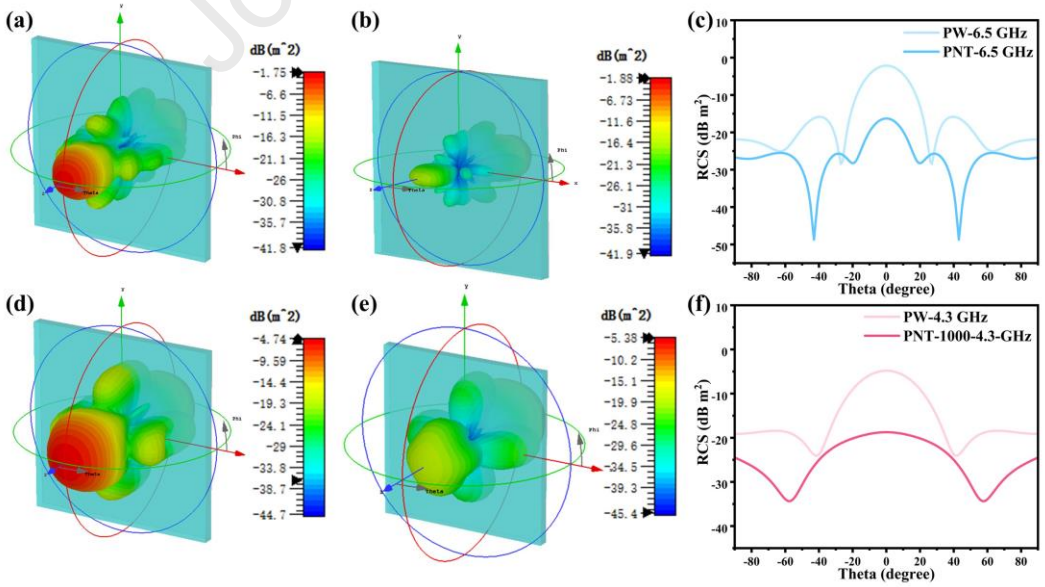

Fig. 6. CST simulation results of (a) PW-6.5 GHz, (b) PNT-6.5 GHz, (d) PW-4.3 GHz, and (e) PNT-1000-4.3 GHz; RCS simulation curve of (c) PW-6.5 GHz and PNT-6.5 GHz (f) PW-4.3 GHz and PNT-1000-4.3 GHz.

3.4. Thermal Conductivity of PNT-X@PDMS Composites

The EWA process mainly converts microwave energy into thermal energy, thus resulting in the accumulation of heat inside the composites. Therefore, it is of crucial importance for the composites to possess excellent thermal conductivity to quickly dissipate the accumulated heat. We mixed PNT-X with PDMS to prepare PNT-X@PDMS composites to verify the thermal conductivity of PNT-X. As shown in Fig. 7 (a), it displays the photos of the PNT-X@PDMS composites, which are black in color and exhibit good flexibility, including the abilities to be folded, rolled and fully restore to their original shapes. This enables them to fit well on the surface of the testing platform, which is beneficial for verifying their thermal effects.

Furthermore, Fig. 7 (b) shows the in-plane thermal conductivity of the PNT-X@PDMS composites. In the PNT-X@PDMS composites, the volume fraction of PNT-X is 10%. Its thermal conductivity increases with the increase in the heat treatment temperature of PNT-X. Notably, the PNT@PDMS and PNT-1000@PDMS composites exhibit thermal conductivities of 1.31 W/(m·K) and 2.26 W/(m·K), respectively. In contrast, the PNT-2000@PDMS composite exhibits exceptional thermal transport properties, achieving a thermal conductivity of 4.20 W/(m·K). This represents a 1589% increase relative to the pristine PDMS matrix (0.26 W/(m·K)). Because, as can be seen from Fig. 2 (a ~ d), the crystallinity of PNT-2000 is higher than that of PNT-1000 and PNT, while the defect I_D/I_G value is much lower than that of PNT-1000 and PNT. This indicates

that as the heat treatment temperature of PNT-X increases, the grain size increases and the number of defects decreases. The enlarged grains provide more continuous and efficient phonon transmission channels, which is beneficial for improving the thermal conductivity [78]. Therefore, PNT-X@PDMS exhibits excellent thermal conductivity.

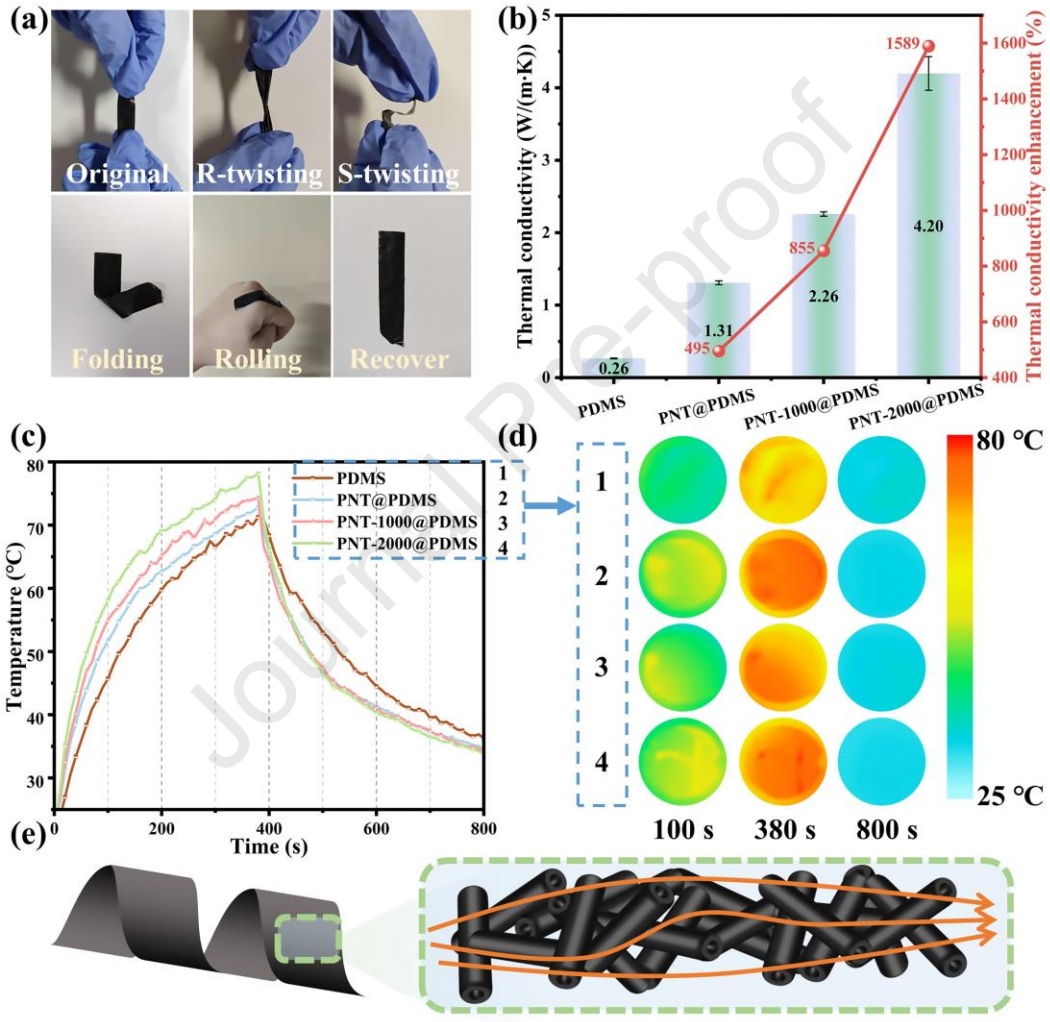

Fig. 7. (a) The flexibility of PNT-X@PDMS composites. (b) The thermal conductivites of PNT-X@PDMS composites, (c) infrared thermal images and (d) temperature-time curves, (e) thermal conduction mechanisms.

Thermal response characteristics were evaluated through temperature-time profiling and infrared thermography. Fig. 7 (c, d) show that the heating rates progressively increased during the

380 s heating process. When the temperature of the PDMS reached 71.3 ºC, the PNT@PDMS, PNT-1000@PDMS, and PNT-2000@PDMS composite reached 72.8 ºC, 74.3 ºC, and 78.2 ºC, respectively. Subsequently, at the same cooling time, the temperatures of the PNT@PDMS, PNT-1000@PDMS, and PNT-2000@PDMS decreased to 38.9 ºC, 35.4 ºC and 33.8 ºC respectively. This is because PNT-X is uniformly dispersed in the PDMS matrix (Fig. S8). When PNT-X achieves sufficient overlap in the PDMS matrix, it facilitates the formation of a thermal conductive network (Fig. 7 (e)), thereby significantly improving the thermal conductivity of the PNT-X@PDMS composites. Therefore, the heat transfer efficiency of the PNT-X@PDMS composites are higher, leading to a faster temperature decline.

4. Conclusion

In summary, this study demonstrates a straightforward and efficient Joule heat-driven carbonization method to control the ratio of amorphous phase to graphite phase in polymer nanotubes, thereby significantly improving their EWA performance. The transformation of nitrogen-containing defects promotes polarization relaxation, defect formation, and dipole polarization, which together improve charge transfer and achieve excellent absorption performance. The optimized material exhibits an EAB of 3.46 GHz and a minimum RL of −45.1 dB at 1000 ºC. At higher temperatures of 1500 ºC, nitrogen-containing defects are gradually eliminated, and vacancy defects decrease, which impairs the EWA performance. When the temperature reaches 2000 ºC, adding 10 wt% PNT-2000 to PDMS results in a remarkable thermal conductivity of 4.20 W/(m·K). This value corresponds to a 1589% increase relative to pristine

PDMS. This work establishes an effective design strategy for developing multifunctional composites capable of addressing EWA and thermal management requirements in advanced electronic applications challenged by increasing electromagnetic radiation.

Declaration of competing interest

The authors declare that they have no known competing financial interests or personal relationships that could have appeared to influence the work reported in this paper.

Acknowledgements

This work was supported by the National Natural Science Foundation of China (Grant No. 52003111, 21975054 and U20A20340), National Key R&D Program of China (2020YFB0408100), Anhui Provincial Key Research and Development Project (2023z04020021), the Program for Guangdong Introducing Innovative and Entrepreneurial Team (2016ZT06C412), Foshan Science and Technology Innovation Team Project (1920001000108). The authors extend their appreciation to Taif University, Saudi Arabia for supporting this work through project number (TU-DSPP-2025-19).

References

[1] S. Gite, U. Rawat, S. Kumar, B. Saini, A. Bhatt, K. Kotecha, N. Naik, Unfolding Conversational Artificial Intelligence: A Systematic Review of Datasets, Techniques and Challenges in Developments, Eng. Sci. 31 (2024) 1210.

[2] X.J.K. Ng, A.S. Mohd Khairuddin, H.C. Liu, T.C. Loh, J.L. Tan, S.M. Khor, B.F. Leo, Artificial intelligence-assisted point-of-care devices for lung cancer, Clinica Chimica Acta 570 (2025) 120191.

[3] B. Chen, J. Dong, M. Ruelas, X. Ye, J. He, R. Yao, Y. Fu, Y. Liu, J. Hu, T. Wu, C. Zhou, Y. Li, L. Huang, Y.S. Zhang, J. Zhou, Artificial intelligence-assisted high-throughput screening of printing conditions of hydrogel architectures for accelerated diabetic wound healing, Adv. Funct. Mater. 32(38) (2022) 2201843.

[4] S. Bunian, M.A.A. Al-Ebrahim, A.A. Nour, Role and Applications of Artificial Intelligence and Machine Learning in Manufacturing Engineering: A Review, Eng. Sci. 29 (2024) 1088.

[5] J.-M. Kim, K.H. Lee, J.Y. Lee, Extracting polaron recombination from electroluminescence in organic light-emitting diodes by artificial intelligence, Adv. Mater. 35(14) (2023) 2209953.

[6] M. Sudhi, V.K. Shukla, D.K. Shetty, V. Gupta, A.S. Desai, N. Naik, B.M.Z. Hameed, Advancements in Bladder Cancer Management: A Comprehensive Review of Artificial Intelligence and Machine Learning Applications, Eng. Sci. 26 (2023) 1003.

[7] R.R. Hasan, J. Jasmine, A.M. Saleque, S.H. Eshan, R.T.H. Tusher, S. Zabin, N. Nowshin, M.A. Rahman, Y.H. Tsang, Spin coated multi-walled carbon nanotube patch antenna for breast cancer detection, Adv. Mater. Technol. 8(24) (2023) 2300822.

[8] S. Khotthada, A. Matthujak, P. Khamphakdi, J. Glinubon, C. Siriboon, I. Salangam, S. Phongthanapanich, Development and Performance Analysis of an Electromagnetic Needle-Free Jet Injection Device for Efficient Drug Delivery in Pig Farms, Eng. Sci. 33 (2025) 1329.

[9] P. Vengsungnle, J. Jongpleumpiti, N. Naphon, S. Poojeera, A. Srichat, S.E. Eiamsa-ard, P. Naphon, Oscillating Electromagnetic Field Effect on Nusselt Number and Pressure Drop of Ferrofluid in the Fluted Tubes, Eng. Sci. 32 (2024) 1307.

[10] X. He, C. Cui, Y. Chen, L. Zhang, X. Sheng, D. Xie, MXene and polymer collision: sparking the future of high-performance multifunctional coatings, Adv. Funct. Mater. 34(51) (2024) 2409675.

[11] Q. Zheng, J. Wang, W. Cao, H. Zhai, M. Cao, Hetero-dimensional micro-nano architectures toward electromagnetic devices and hybrid energy transport, Adv. Funct. Mater. 35(13) (2025) 2417972.

[12] P. Vengsungnle, S. Poojeera, A. Srichat, P. Naphon, Optimized Performance of Closed Loop Control Electromagnetic Field for the Electric Generators with Energy Storage, Eng. Sci. 30 (2024) 1173.

[13] D.B. Kadyrzhanov, M.E. Kaliyekperov, A.T. Zhumazhanova, A.L. Kozlovskiy, Study of the Application Prospects of Metal Oxide Films as Protective Materials for Electron Radiation

Shielding, ES Mater. Manuf. 25 (2024) 1231.
[14] Y. Ruihan, L. Qianhui, Y. Kaijie, Z. Li, C. Ying, H. Zan, S. Xinxin, Construction strategies and recent advances of flexible EMI phase change composites, Soft Sci. 5(1) (2025) 8.
[15] J. Cheng, Y. Jin, J. Zhao, Q. Jing, B. Gu, J. Wei, S. Yi, M. Li, W. Nie, Q. Qin, D. Zhang, G. Zheng, R. Che, From VIB- to VB-group transition metal disulfides: structure engineering modulation for superior electromagnetic wave absorption, Nano-Micro Lett. 16 (1) (2023) 29.
[16] M. Zhou, S. Zhang, L. Zhang, Y. Chen, X. Sheng, X. Zhang, Integration of MXene and polymer: Unlocking the full potential of multifunctional composites for electromagnetic interference shielding, J. Mater. Sci. Technol. 226 (2025) 12-35.
[17] M. He, J. Hu, H. Yan, X. Zhong, Y. Zhang, P. Liu, J. Kong, J. Gu, Shape Anisotropic Chain-Like CoNi/Polydimethylsiloxane Composite Films with Excellent Low-Frequency Microwave Absorption and High Thermal Conductivity, Adv. Funct. Mater. 35 (2024) 2316691.
[18] X. Zhong, M. He, C. Zhang, Y. Guo, J. Hu, J. Gu, Heterostructured BN@Co-C@C Endowing Polyester Composites Excellent Thermal Conductivity and Microwave Absorption at C Band, Adv. Funct. Mater. 34 (2024) 2313544.
[19] M. He, X. Zhong, X. Lu, J. Hu, K. Ruan, H. Guo, Y. Zhang, Y. Guo, J. Gu, Excellent Low-Frequency Microwave Absorption and High Thermal Conductivity in Polydimethylsiloxane Composites Endowed by Hydrangea-Like CoNi@BN Heterostructure Fillers, Adv. Mater. 36(48) (2024) 2410186.
[20] L. Zhou, P. Hu, M. Bai, N. Leng, B. Cai, H.-L. Peng, P.-Y. Zhao, Y. Guo, M. He, G.-S. Wang, J. Gu, Harnessing the Electronic Spin States of Single Atoms for Precise Electromagnetic Modulation, Adv. Mater. 37(7) (2025) 2418321.
[21] F. Xiao-Xuan, Z. Xin-Ci, L. Lin, C. Mao-Sheng, Recent progress and perspective of microwave absorption materials derived from metal-organic frameworks, Soft Sci. 4(4) (2024) 43.
[22] Y. Zhong, D. Liu, Q. Yang, Y. Qu, C. Yu, K. Yan, P. Xie, X. Qi, Z. Guo, Z. Toktarbay, Boosting microwave absorption performance of bio-gel derived Co/C nanocomposites, Eng. Sci. 26 (2023) 988.
[23] D. Sheng, Z. Song, S. Cheng, W. Wang, Z. Chen, R. Gao, W. Li, A. Xie, Defect-rich carbon nanosheets derived from $p(C_3O_2)_x$ for electromagnetic wave absorption applications, Carbon 230 (2024) 119637.
[24] W. Huang, M. Song, S. Wang, B. Wang, J. Ma, T. Liu, Y. Zhang, Y. Kang, R. Che, Dual-step redox engineering of 2D CoNi-alloy embedded B, N-doped carbon layers toward tunable electromagnetic wave absorption and light-weight infrared stealth heat insulation devices, Adv. Mater. 36(30) (2024) 2403322.
[25] X. Xiong, H. Zhang, H. Lv, L. Yang, G. Liang, J. Zhang, Y. Lai, H.-W. Cheng, R. Che, Recent progress in carbon-based materials and loss mechanisms for electromagnetic wave absorption, Carbon 219 (2024) 118834.

[26] W. Yu, Z. Wang, J. Lin, Y. Xiao, L. Zhu, J. Huang, A. Pereira, Z. Guo, Y. Min, Rose-derived porous carbon and in-situ fabrication of cobalt/nickel nanoparticles composites as high-performance electromagnetic wave absorber, Eng. Sci. 30 (2024) 1113.

[27] C. Wu, J. Wang, X. Zhang, L. Kang, X. Cao, Y. Zhang, Y. Niu, Y. Yu, H. Fu, Z. Shen, K. Wu, Z. Yong, J. Zou, B. Wang, Z. Chen, Z. Yang, Q. Li, Hollow gradient-structured iron-anchored carbon nanospheres for enhanced electromagnetic wave absorption, Nano-Micro Lett. 15 (1) (2022) 7.

[28] L.T. Nguyen, C.J. Goh, T. Bai, R.H. Ong, X.Y. Goh, H.M. Duong, Scalable fabrication of lightweight carbon nanotube aerogel composites for full X-band electromagnetic wave absorption, Carbon 219 (2024) 118811.

[29] Z. Chen, J. Zhang, L. Ni, D. Sheng, R. Gao, W. Li, A. Xie, Improving electromagnetic wave absorption property of metal borides/carbon nanocomposites by magnetic-electric balance and ion substitution tuning strategy, Carbon 221 (2024) 118901.

[30] X. He, W. Zhang, Y. Yang, G. Yang, Y. Zhang, G. Huang, J. Luo, C. Cui, X. Sheng, Triple-network structured phase change composite based on “rod-brush” CNTs-CFs with high thermal conductivity, Compos. Sci. Technol. 262 (2025) 111080.

[31] K. Zhang, Y. Liu, Y. Liu, Y. Yan, G. Ma, B. Zhong, R. Che, X. Huang, Tracking regulatory mechanism of trace Fe on graphene electromagnetic wave absorption, Nano-Micro Lett. 16 (1) (2024) 66.

[32] C. Liu, J. Lin, N. Wu, C. Weng, M. Han, W. Liu, J. Liu, Z. Zeng, Perspectives for electromagnetic wave absorption with graphene, Carbon 223 (2024) 119017.

[33] Z. Mai, K. You, J. Chen, X. Sheng, Y. Chen, Biomass lignin/manganese ferrite-modified reduced graphene oxide aerogel composites for multi-source energy conversion, Int. J. Biol. Macromol. 306 (2025) 141688.

[34] J. Yan, Z. Ye, W. Chen, P. Liu, Y. Huang, Metal Mo and nonmetal N, S co-doped 3D flowers-like porous carbon framework for efficient electromagnetic wave absorption, Carbon 216 (2024) 118563.

[35] S. Wang, Q. Liu, S. Li, F. Huang, H. Zhang, Joule-heating-driven synthesis of a honeycomb-like porous carbon nanofiber/high entropy alloy composite as an ultralightweight electromagnetic wave absorber, ACS Nano 18 (6) (2024) 5040-5050.

[36] X. Ge, G. Tay, Y. Hou, Y. Zhao, P.J. Sugumaran, B.Q. Thai, C.K. Ang, W. Zhai, Y. Yang, Flexible and leakage-proof phase change composite for microwave attenuation and thermal management, Carbon 210 (2023) 118084.

[37] Y. Lin, B. Zhong, J. Chen, B. Zhang, Y. Yu, Reinforcement of microwave absorption and thermal conductivity of polydimethylsiloxane achieved by metal-organic framework-derived carbon nanotube/boron nitride flake heterogeneous structure, Carbon 227 (2024) 119242.

[38] J. Guo, S. Xi, Y. Zhang, X. Li, Z. Chen, J. Xie, X. Zhao, Z. Liu, H. Colorado, H. H, o. Li, Z.M.E. El-Bahy, W. Abdul, J. Zhu, Biomass-based Electromagnetic Wave Absorption Materials with Unique Structures: A Critical Review, ES Food Agrofor. 13 (2023) 900.

[39] B. Dai, J. Li, X. Liu, N. Wang, Y. Dai, Y. Qi, Multiple synergistic losses in the absorption of electromagnetic waves by three-dimensional cross-linked carbon fiber, Carbon 195 (2022) 308-318.

[40] H. Xu, M. Liu, Z. Ma, B. Kang, X. Zhang, C. Zhu, X. Zhang, Y. Chen, Zn,N-codoped mesoporous carbon particles/carbon fibers for wide-band electromagnetic wave absorption, Chem. Eng. J. 479 (2024) 147666.

[41] A. Cornelio, E. Galli, M. Scaglia, A. Zanoletti, A. Zacco, A. Bonometti, G. Magugliani, E. Mossini, E. Macerata, S. Federici, E. Bontempi, Recovery of NMC-lithium battery black mass by microwave heating processes, Energy Storage Mater. 72 (2024) 103703.

[42] S. Vongpradubchai, N. Makul, P. Rattanadecho, Novel Microwave-Assisted Drying Technique for Thai Medicinal Herbs Utilizing an Asymmetrical Double-Feed Microwave/Vacuum System, Eng. Sci. 32 (2024) 1273.

[43] W. Klinbun, P. Rattanadecho, A computational analysis of how the design of multicompartment containers and placement angle affect heat and mass transfer during the microwave heating process, Eng. Sci. 26 (2023) 970.

[44] W. Shi, Z. Li, Z. Gong, Z. Liang, H. Liu, Y.-C. Han, H. Niu, B. Song, X. Chi, J. Zhou, H. Wang, B.Y. Xia, Y. Yao, Z.-Q. Tian, Transient and general synthesis of high-density and ultrasmall nanoparticles on two-dimensional porous carbon via coordinated carbothermal shock, Nat. Commun. 14 (1) (2023) 2294.

[45] J. Huang, S. Zhu, J. Zhang, G. Han, One-pot ultrafast molten-salt synthesis of anthracite-based porous carbon for high-performance capacitive energy storage, ACS Mater. Lett. 6 (6) (2024) 2144-2152.

[46] K.H. Baloch, N. Voskanian, M. Bronsgeest, J. Cumings, Remote Joule heating by a carbon nanotube, Nat. Nanotechnol. 7 (5) (2012) 316-319.

[47] Y. Chen, Q. He, Y. Zhao, W. Zhou, P. Xiao, P. Gao, N. Tavajohi, J. Tu, B. Li, X. He, L. Xing, X. Fan, J. Liu, Breaking solvation dominance of ethylene carbonate via molecular charge engineering enables lower temperature battery, Nat. Commun. 14 (1) (2023) 8326.

[48] M. He, G. Wang, Y. Zhu, Y. Wang, F. Liu, S. Luo, In-situ joule heating-triggered nanopores generation in laser-induced graphene papers for capacitive enhancement, Carbon 186 (2022) 215-226.

[49] J. Yang, J. Lin, S. Sun, X. Li, L. Liu, C. Wang, Multidimensional network of polypyrrole nanotubes loaded with ZIF-67 to construct multiple proton transport channels in composite proton exchange membranes for fuel cells, J. Mater. Sci. Technol. 152 (2023) 75-85.

[50] X. Feng, Z. Yan, R. Li, X. Liu, W. Hou, The synthesis of shape-controlled polypyrrole/graphene and the study of its capacitance properties, Polym. Bull. (Berlin) 70 (8) (2013) 2291-2304.

[51] H. Xiang, C. Xin, Z. Hu, L. Aigouy, Z. Chen, X. Yuan, Long-term stable near-infrared–short-wave-infrared photodetector driven by the photothermal effect of polypyrrole nanostructures, ACS Appl. Mater. Interfaces 13(38) (2021) 45957-45965.

[52] C. Esmaeili, M. Ghasemi, L.Y. Heng, S.H.A. Hassan, M.M. Abdi, W.R.W. Daud, H. Ilbeygi, A.F. Ismail, Synthesis and application of polypyrrole/carrageenan nano-bio composite as a cathode catalyst in microbial fuel cells, Carbohydr. Polym. 114 (2014) 253-259.

[53] Y. Wu, S. Tan, G. Fang, Y. Zhang, G. Ji, Manipulating CNT films with atomic precision for absorption effectiveness–enhanced electromagnetic interference shielding and adaptive infrared camouflage, Adv. Funct. Mater. 35 (2024) 2402193.

[54] Z. Sun, Z. Liu, B. Han, Y. Wang, J. Du, Z. Xie, G. Han, Fabrication of ruthenium–carbon nanotube nanocomposites in supercritical water, Adv. Mater. 17 (7) (2005) 928-932.

[55] M. Weng, X. Luo, L. Jian, J. Liang, J. Hu, Y. Liu, J. Zhang, X. Feng, Y. Min, Lutidine catalyzed highly thermal conductive graphite polyimide films via controlling grain size, Appl. Surf. Sci. 578 (2021) 152029.

[56] C. Han, J. Lee, H. Chang, Thermal annealing effects on structure and morphology of micrometer-sized carbon tubes, Chem. Mater. 13 (11) (2001) 4180-4186.

[57] J. Huang, H. Lv, X. Zhao, J.M. Lee, Y. Min, Effect of deep eutectic solvent on the graphitization and thermal properties of polyimide films, J. Appl. Polym. Sci. 142 (2025) e56879.

[58] J. Yin, J. Jin, C. Chen, Y. Lei, Z. Tian, Y. Wang, Z. Zhao, A.-H. Emwas, Y. Zhu, Y. Han, U. Schwingenschlögl, W. Zhang, H.N. Alshareef, Preferential pyrolysis construction of carbon anodes with 8400 h lifespan for high-energy-density K-ion batteries, Angew. Chem. 135 (17) (2023) e202301396.

[59] J. Huang, Y. Chen, Z. Cen, T. Yi, M. Liang, Y. Zhu, R. Liu, R. Fu, S. Liu, D. Wu, Topological defect-regulated porous carbon anodes with fast interfacial and bulk kinetics for high-rate and high-energy-density potassium-ion batteries, Adv. Mater. 36 (30) (2024) 2403033.

[60] M. Oubella, S.B. Jadi, M. El Fazdoune, K. Bahend, E.A. Bazzaoui, J.I. Martins, R. Wang, J.E. de la Rosa, F.J. Garcia-Garcia, M. Bazzaoui, Effect of surface pretreatment on the polypyrrole coating of acrylonitrile butadiene styrene. Part A: Synthesis and characterization, Prog. Org. Coat. 195 (2024) 108654.

[61] T. Kuanyshbekov, N. Guseinov, B. Kurbanova, R. Nemkaeva, K. Akatan, Z. Tolepov, M. Tulegenova, M. Aitzhanov, E. Zhasasynov, S. Thomas, Local natural graphite as a promising raw material for the production of thermally reduced graphene-like films, ES Mater. Manuf. 23 (2024) 1000.

[62] P. Zhang, J. Fan, Y. Wang, Y. Dang, S. Heumann, Y. Ding, Insights into the role of defects on the Raman spectroscopy of carbon nanotube and biomass-derived carbon, Carbon 222 (2024) 118998.

[63] C. Han, J. Lee, R. Yang, C. Han, Formation mechanism of micrometer-sized carbon tubes, Chem. Mater. 13 (8) (2001) 2656-2665.

[64] S. Lee, Y. Hwang, T. Byun, J. Ko, J. Roh, Effect of heating rate, temperature, and residence time during graphitization on the mechanical and electrical properties of isotropic graphite blocks, Carbon 208 (2023) 443-451.

[65] A. Xie, F. Wu, W. Jiang, K. Zhang, M. Sun, M. Wang, Chiral induced synthesis of helical polypyrrole (PPy) nano-structures: a lightweight and high-performance material against electromagnetic pollution, J. Mater. Chem. C 5 (8) (2017) 2175-2181.

[66] Y. Peng, B. Guo, W. Wang, P. Yu, Z. Wu, L. Shao, W. Luo, Efficient preparation of nitrogen-doped lignin-based carbon nanotubes and the selectivity of nitrogen speciation for photothermal therapy, Int. J. Biol. Macromol. 238 (2023) 124127.

[67] J. Cheng, H. Zhang, M. Ning, H. Raza, D. Zhang, G. Zheng, Q. Zheng, R. Che, Emerging materials and designs for low- and multi-band electromagnetic wave absorbers: the search for dielectric and magnetic synergy?, Adv. Funct. Mater. 32 (23) (2022) 2200123.

[68] X. Li, X. Wang, M. Li, W. Zhu, H. Luo, X. Lu, H. Xu, J. Xue, F. Ye, H. Wu, X. Fan, Built-in electric field enhancement strategy induced by cross-dimensional nano-heterointerface design for electromagnetic wave absorption, Adv. Funct. Mater. (2024) 2407217.

[69] Y. Kang, J. Tang, J. Chen, M. Song, W. Wang, T. Liu, W. Huang, "Appropriate dressing" non-fluorination strategy: Dopamine coating $CuSiF_6$ framework derived F-rich SiC/CuF_2@C electromagnetic wave absorber, Carbon 218 (2024) 118690.

[70] Y. Yang, Z. Xiu, F. Pan, H. Liang, H. Jiang, H. Guo, X. Wang, L. Li, B. Yuan, W. Lu, Tuning the multilevel hierarchical microarchitecture of MXene/rGO-based aerogels through a magnetic field-guided strategy toward stepwise enhanced electromagnetic wave dissipation, Adv. Funct. Mater. (2024) 2406133.

[71] T. Liu, C. Wang, X. Zhang, H. Huo, H. Li, W. Zhang, M. Ren, C. Yan, H. Huang, W. Huang, Phase engineering in a twin-phase β/γ-MoCx lightweight nanoflower with matched fermi level for enhancing electron transport across the polarized interfaces in electromagnetic wave attenuation, Adv. Funct. Mater. 34(51) (2024) 2410194.

[72] X. Wang, B. Wang, H. Zhu, B. Cao, T. Liu, A nanoconfinement strategy to construct Co@CNTs for lightweight and ultra-broadband microwave absorption, Small 20 (47) (2024) 2405351.

[73] B. Li, Z. Ma, X. Zhang, J. Xu, Y. Chen, X. Zhang, C. Zhu, NiO/Ni heterojunction on N-doped hollow carbon sphere with balanced dielectric loss for efficient microwave absorption, Small 19 (12) (2023) 2207197.

[74] S. Zhang, D. Lan, J. Zheng, J. Kong, J. Gu, A. Feng, Z. Jia, G. Wu, Perspectives of nitrogen-doped carbons for electromagnetic wave absorption, Carbon 221 (2024) 118925.

[75] S. Cheng, D. Sheng, S. Mukherjee, W. Dong, Y. Huang, R. Cao, A. Xie, R.A. Fischer, W. Li, Carbon nanolayer-mounted single metal sites enable dipole polarization loss under electromagnetic field, Nat. Commun. 15(1) (2024).

[76] Z. Hou, X. Gao, J. Zhang, G. Wang, A perspective on impedance matching and resonance absorption mechanism for electromagnetic wave absorbing, Carbon 222 (2024) 118935.

[77] Y. Tian, M. Huang, N. Kong, Z. Wang, C. Ye, L. Fu, K. Jia, J. Fan, R. Tan, F. Han, Designing insulative SiC coating layer on the artificial graphite particle to achieve synergy of wave absorption and thermal conduction, Carbon 214 (2023) 118352.

[78] J. Wang, Z. Wang, K. Yang, N. Chen, J. Ni, J. Song, Q. Li, F. Sun, Y. Liu, T. Fan, Enhanced heat transport capability across boron nitride/copper interface through inelastic phonon scattering, Adv. Funct. Mater. 32 (40) (2022) 2206545.

Declaration of interests

☒ The authors declare that they have no known competing financial interests or personal relationships that could have appeared to influence the work reported in this paper.

☐The authors declare the following financial interests/personal relationships which may be considered as potential competing interests: